# Selective Covalent Targeting of SARS-CoV-2 Main Protease by Enantiopure Chlorofluoroacetamide

Daiki Yamane[†], Satsuki Onitsuka[†], Suyong Re[‡], Hikaru Isogai[†], Rui Hamada[†], Tadanari Hiramoto[†], Eiji Kawanishi[†], Kenji Mizuguchi[‡], Naoya Shindo[†*], Akio Ojida[†*]

[†]Graduate School of Pharmaceutical Sciences, Kyushu University, 3-1-1 Maidashi, Hikashi-ku, Fukuoka 812-8582, Japan

[‡]Artificial Intelligence Center for Health and Biomedical Research, National Institute of Biomedical Innovation, Health, and Nutrition, 7-6-8 Saito-Asagi, Ibaraki, Osaka 567-0085, Japan

*Corresponding authors:     shindo708@phar.kyushu-u.ac.jp (N.S.)

ojida@phar.kyushu-u.ac.jp (A.O.)

**Abstract**

The pandemic of COVID-2019 has urged the development of antiviral agents against its causative pathogen SARS-CoV-2. The main protease ($M^{pro}$), a cysteine protease essential for viral replication, is a promising protein target. Here we report an irreversible SARS-CoV-2 $M^{pro}$ inhibitor possessing chlorofluoroacetamide (CFA) as the warhead for covalent modification of $M^{pro}$. Ugi multi-component reaction employing chlorofluoroacetic acid allowed rapid generation of CFA derivatives, of which diastereomers displayed significantly different inhibitory activity against $M^{pro}$. We established a protocol for the optical resolution of chlorofluoroacetic acid, which enable the isolation of the stereoisomers of the best CFA compound **18**. Kinetic analysis revealed that ($R$)-CFA is crucial for both binding affinity and the rate of irreversible inactivation. Our findings highlight the prominent influence of the CFA chirality on the covalent modification of cysteine, and provide the basis for improving the potency and selectivity in the development of novel CFA-based covalent inhibitors.

**Keywords:** SARS-CoV-2, main protease, chlorofluoroacetamide, Ugi multi-component reaction, cysteine

## Introduction

The outbreak of the novel coronavirus disease 2019 (COVID-19), caused by severe acute respiratory syndrome coronavirus 2 (SARS-CoV-2),[1,2] has been posing a serious threat to the global public health and economy. Although efficacious vaccines are now being administered worldwide, novel SARS-CoV-2 variants of interest and concern continue to emerge.[3] Thus, the development of antiviral agents against SARS-CoV-2 is urgently needed to put an end to the current pandemic.[4,5] SARS-CoV-2 has a positive-sense single-stranded genomic RNA that encodes polyproteins pp1a and pp1ab. Two cysteine proteases, the main protease (M[pro], also known as 3C-like protease, 3CL[pro]) and the papain-like protease (PL[pro]), are excised from these polyproteins by autocleavage and further digest polyproteins into nonstructural proteins (nsps), including crucial components of the viral replication–translation machinery. While both proteases are essential for viral replication, M[pro] has been extensively studied as an attractive drug target against SARS-CoV-2 owing to the predominant role in polyprotein processing and the lack of a human homolog.[6,7]

M[pro] recognizes glutamine and a hydrophobic amino acid residue at the S1 and S2 pockets in the active site, respectively, and cleaves amide bonds mainly within the Leu-Gln↓(Ser, Ala, Gly) sequence (↓: cleavage site).[8] This substrate specificity is conserved across other coronaviruses, including the causative pathogens of past outbreaks, SARS-CoV-1 and Middle-East respiratory syndrome coronavirus (MERS-CoV).[9,10] Therefore, current efforts to develop SARS-CoV-2 M[pro] inhibitors are greatly aided by the previous compound designs, especially ones targeting SARS-CoV-1 M[pro].[5,6] The majority of SARS-CoV-2 M[pro] inhibitors reported to date are peptidomimetics based on the Leu-Gln sequence, combined with an electrophilic warhead, such as α-ketoamide,[11] aldehyde,[12–15] ketone,[16–19] and vinyl sulfone,[8] for the covalent capture of the sulfhydryl group of catalytic Cys145. PF-00835231, developed by Pfizer, is one of the representative compounds in this category, of which prodrug is now under clinical trials (Figure 1A).[12] The ketone electrophile of this compound allows reversible covalent engagement with M[pro]. Other than peptidomimetics, several dipeptide compounds generated by Ugi multi-component reaction (MCR), are reported as SARS-CoV-1 and SARS-CoV-2 M[pro] inhibitors (Figure 1B).[20–22]
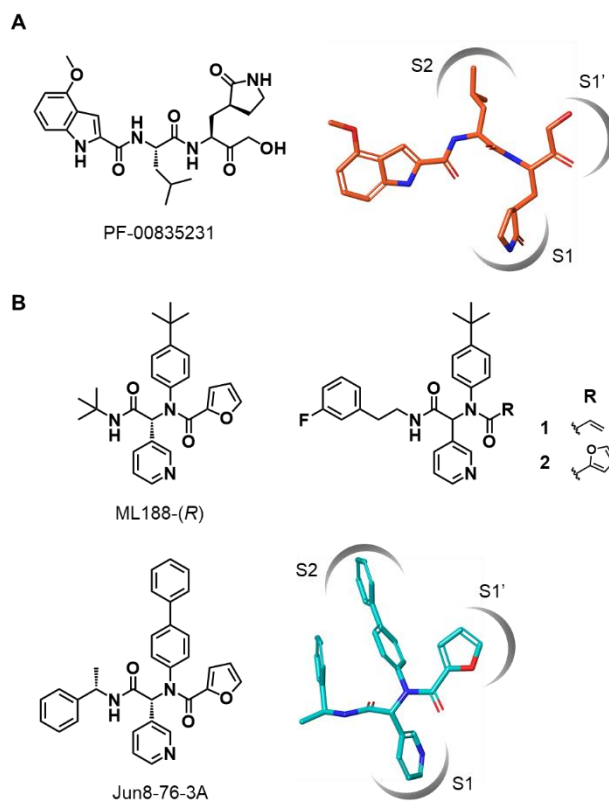
**Figure 1**. Chemical structures of SARS-CoV-2 M[pro] inhibitors. A) The structure of a representative peptidomimetic inhibitor PF-00835231 and its binding mode in the M[pro] active site (The conformation was retrieved from the cocrystal structure, PDB code 6XHM). B) The structures of M[pro] inhibitors based on the Ugi MCR-generated dipeptide scaffold and the binding mode of Jun8-76-3A in the Mpro active site (The conformation was retrieved from the cocrystal structure, PDB code 7KX5).

Covalent inhibition of proteins has been a powerful strategy for achieving potent and sustained pharmacological efficacy.[23] In particular, a number of acrylamide-based covalent inhibitors targeting the noncatalytic cysteine of cancer-associated proteins have been clinically approved or under clinical trials for cancer treatment.[24,25] Nonetheless, care should be taken to ensure a high degree of target selectivity for minimizing the toxicity risk due to nonspecific off-target labeling.[26] Because medications for infectious disease treatment would require a broader margin of safety compared to anticancer agents, this point is crucial for designing covalent M[pro] inhibitors. One strategy for achieving high target selectivity is the use of weakly reactive, or "latent" electrophiles,[27,28] which are stable toward off-target biomolecules but sufficiently reactive under the microenvironment in the binding pocket of the target. Reversible modification of the targeted amino acid residue represents another useful strategy to eliminate undesired inhibitor–protein adducts.[29,30] We have recently introduced α-chloroacetamide (CFA) as a weakly reactive, cysteine-directed warhead useful for covalent inhibition of tyrosine kinases[31,32] and a cysteine protease.[33] The CFA group exhibited weaker intrinsic reactivity toward cysteine thiol than the acrylamides, and the gel-based activity-based protein profiling (ABPP)

experiments revealed that the CFA-based inhibitors exhibited the higher reaction selectivity toward the targeted tyrosine kinase compared to the structurally related acrylamide-based inhibitors. We also demonstrated that the CFA–thiol adduct was gradually hydrolyzed under neutral aqueous conditions to reversibly generate an unmodified free thiol, whereas the CFA–target protein adduct stably existed in the binding pocket sequestered from aqueous solvents. Given these desirable reaction features, we envisioned that CFA-based compound would serve as selective covalent SARS-CoV-2 M[pro] inhibitors.

In the present study, we report the development of CFA-based novel covalent inhibitors against SARS-CoV-2 M[pro]. Ugi MCR using chlorofluoroacetic acid allowed rapid synthesis of CFA-appended dipeptides and fast structure–activity relationship (SAR) study by a fluorescence-based enzymatic assay to provide **18** as the optimized CFA compound. Interestingly, we found that the absolute configuration of the chiral center of CFA unit largely affected the inhibitory activity of **18**. To gain insight into this phenomenon, we established a simple synthetic procedure for enantiomerically pure chlorofluoroacetic acid and prepared the set of four stereoisomers of **18**. Among them, (*R*,*R*)-**18** inhibited M[pro] with a dramatically higher potency than the other isomers. The enzyme kinetics analysis revealed that the *R* configuration of CFA unit of **18** contributes to increasing both the binding affinity and the reaction rate with M[pro], suggesting the importance of the chiral design of CFA unit for enzyme inhibition.

**Results and Discussion**

We chose the dipeptide scaffold, accessible through Ugi MCR, as the starting point of the study. Ugi MCR, a representative multi-component reaction, would generate CFA derivatives in one single step from amine, aldehyde, isocyanide, and chlorofluoroacetic acid. As shown in Figure 1B, several Ugi MCR-generated dipeptides have been reported as M[pro] inhibitors. ML188-(*R*), a SARS-CoV-1 M[pro] inhibitor, was discovered by a high-throughput screen campaign and subsequent structural optimization.[20] Based on this molecular architecture, the group of Chen and Wang recently reported Jun8-76-3A as a SARS-CoV-2 M[pro] inhibitor.[21] Cocrystal structures revealed that the 3-pyridyl group of these compounds interacts with the S1 pocket, which shows a strict selectivity for a glutamine residue of substrates, through hydrogen bonding with His163. 4-*tert*-Butylphenyl or 4-biphenyl group occupies the S2 pocket that prefers hydrophobic amino acid residues such as leucine and phenylalanine. In addition, the furan-2-carboxamide moiety forms a bifurcated interaction with the backbone NH of Gly143 in the S1' pocket. While these compounds reversibly bind to M[pro], London *et al.* reported an acrylamide-based covalent inhibitor **1**, although the potency did not significantly differ from a noncovalent furan-2-carboxamide **2**.[22]

As the initial step, we prepared the CFA analog of **1**. Ugi MCR using racemic chlorofluoroacetic acid proceeded smoothly to afford CFA dipeptide **3**, of which diastereomers could be separated by silica gel chromatography (Figure 2A) (Hereafter, the diastereomer that elutes first in normal-phase chromatography is referred to as A, and the later B). The inhibitory activity of compounds against SARS-CoV-2 M[pro] was assessed by an enzymatic assay using the purified recombinant protein and a fluorogenic substrate Ac-Abu-Tle-Leu-Gln-(4-methylcoumaryl-7-amide) (MCA). This substrate is based on the optimized tetrapeptide sequence reported

120 by Drag *et al.*[8] and allows robust fluorescent reading compared to the FRET-based substrate possessing an

121 Edans/Dabcyl donor–acceptor pair.[34] We found that the diastereomers **3A** and **3B** displayed significantly

122 different inhibitory activity against SARS-CoV-2 $M^{pro}$ (Figure 2B). Whereas **3A** was virtually inactive ($IC_{50} >$

123 20 μM), **3B** exhibited higher inhibitory activity ($IC_{50} = 1.05$ μM) than acrylamide **1** ($IC_{50} = 2.62$ μM). This result

124 was intriguing because it indicated that the $M^{pro}$ inhibitory activity of **3** is sensitive to the chirality of both CFA

125 and the new α-amino acid stereocenter formed by Ugi MCR. Previous studies have shown that the *R*

126 configuration of the amino acid α-carbon of ML188 and Jun8-76-3A is crucial for $M^{pro}$ inhibition. We also

127 assessed the $M^{pro}$ inhibitory activity of acetamide **4** and difluoroacetamide **5** and found that both compounds

128 were inactive ($IC_{50} > 20$ μM). These data, taken together, strongly suggest that the covalent attachment at CFA

129 contributes to the $M^{pro}$ inhibitory activity of **3B** in a stereospecific manner.

130
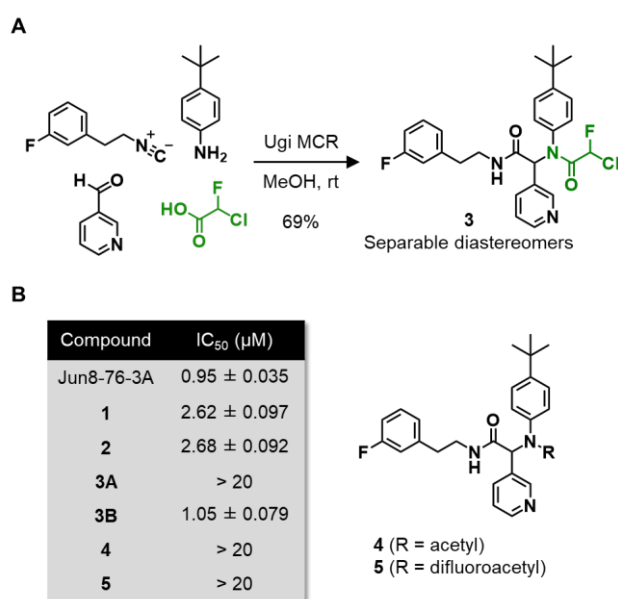


131
132

133 **Figure 2**. A) Preparation of the diastereomers of **3** by Ugi MCR. B) Inhibitory activity of Ugi MCR-generated

134 dipeptides against recombinant SARS-CoV-2 $M^{pro}$. The reported $IC_{50}$ values for Jun8-76-3A, **1**, and **2** are 0.31,

135 2.95, 2.72 μM, respectively.

136
137

138     Encouraged by this result, we next conducted SAR study to improve the potency of CFA dipeptides (Figure

139 3A). We first evaluated the effect of the *para*-substituent on the aniline-derived benzene ring ($R^1$). As this moiety

140 is supposed to occupy the S2 pocket that mainly accommodates a leucine residue, we screened several

141 hydrophobic substituents. The diastereomers of **6–9** were separable by silica gel column chromatography and

142 assayed individually. In all cases, the diastereomer A was inactive ($IC_{50} > 20$ μM). Both a smaller or a larger

143 alkyl group compared to *tert*-butyl at this position reduced the potency (**6B** and **7B**, $IC_{50} = 2.42$ and 2.68 μM,

144 respectively). **8B** possessing a trifluoromethyl group was also less active ($IC_{50} = 3.44$ μM) than **3B**. On the other

145 hand, the $M^{pro}$ inhibitory activity of **9B** carrying a pentafluorosulfanyl ($SF_5$) group, a thermally and chemically

stable bioisostere for a *tert*-butyl group,[35] was found slightly higher (IC$_{50}$ = 0.90 μM) than that of **3B**. We next investigated the effect of the heterocycle derived from the aldehyde building block (R$^2$). When an additional nitrogen atom was installed to the 3-pyridyl group, we observed increased M$^{pro}$ inhibitory activity except for 3-pyridazinyl derivative **10** (a distereomixture, IC$_{50}$ > 20 μM). 4-pyridazine **11** and 2-pyrazine **13** were assayed as mixtures of diastereomers and showed IC$_{50}$ values of 0.75 and 0.30 μM, respectively. 5-Pyrimidine **12** was the only compound of which diastereomers were separable, and **12B** exhibited the highest activity in the series (IC$_{50}$ = 0.25 μM). The effect of the isocyanide-derived substituent R$^3$ was also investigated. A *tert*-butyl group at this position, as can be seen in the structure of ML188-(*R*), reduced the potency (**14B**, IC$_{50}$ = 3.44 μM). Replacement of the 3-fluorophenyl group with a 3-pyridyl group slightly increased activity (**16**, IC$_{50}$ = 0.73 μM), although the diastereomers were inseparable. Introduction of another benzene ring to **16** afforded a separable diastereomixture of **17**, however, with a slight loss of activity (IC$_{50}$ = 1.43 μM). Finally, considering the M$^{pro}$ inhibitory activity and the separability of diastereomers, we synthesized CFA **18** by employing 4-SF$_5$-phenyl group at R$^1$, 5-pyrimidine at R$^2$, and 2-(3-fluorophenyl)ethyl group at R$^3$ positions, respectively (Figure 3B). **18B** exhibited the most potent M$^{pro}$ inhibitory activity among the tested CFA derivatives with IC$_{50}$ value of 0.22 μM, although this value was not significantly different from that of **12B**. At this point, we determined the relative configuration of the diastereomers of **18**. X-ray crystallography revealed that **18B** has a *syn*-configuration, where the 5-pyrimidinyl group and the CFA fluorine atom orient toward the same direction in the drawn structure (Figure S1). Consequently, **18A** was determined to be an *anti*-isomer.
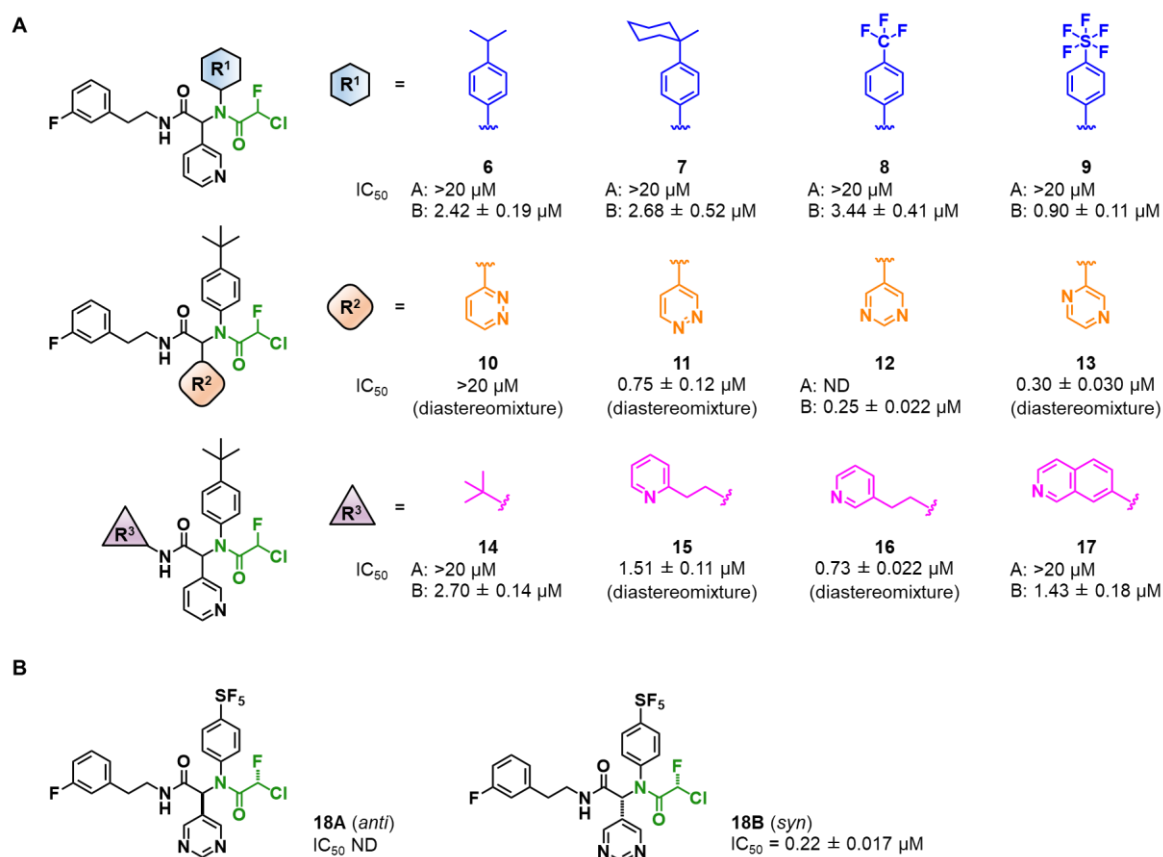
**Figure 3**. Structure–activity relationship of CFA dipeptides. A) Screening of R[1], R[2], and R[3] substituents for the improvement of the inhibitory activity against SARS-CoV-2 M[pro]. ND, not determined. B) Best CFA dipeptide **18** and the relative configuration of each diastereomer determined by X-ray crystallography of **18B** (see Figure S1).

To obtain the four stereoisomers of **18** in pure form, we next focused on the optical resolution of chlorofluoroacetic acid.[36] Wakselman previously reported the preparation of optically active chlorofluoroacetyl chloride based on the chromatographic separation of the diastereomers of CFA **19** derived from (*S*)-(−)-1-phenethylamine.[37] We sought the optical resolution of chlorofluoroacetic acid by a similar approach, however, the isolation of diastereomers of **19** was found laborious in our attempts due to poor separation by silica gel chromatography. Instead, we established a practical procedure to obtain enantiomerically pure chlorofluoroacetic acid employing (*R*)-(−)-2-phenylglycinol (**20**) as the resolving agent (Scheme 1). **20** and commercially available ethyl chlorofluoroacetate were mixed without solvent to afford a diastereomeric mixture of CFA **21**, which was directly charged on silica gel and subjected to chromatography. The diastereomers **21A** and **21B** exhibited much improved separation compared to those of **19**, and each diastereomer was isolated in multigram scale by a single chromatography. The absolute configuration at CFA was determined to be *R* for **21B** by X-ray crystallography (Figure S2). Pure **21A** and **21B** were subjected to hydrolysis in refluxing 3M H$_2$SO$_4$/1,4-dioxane to provide (*S*)- and (*R*)-chlorofluoroacetic acid, respectively. Finally, Ugi MCR using each enantiomer of chlorofluoroacetic acid enabled isolation of the four stereoisomers of **18**.
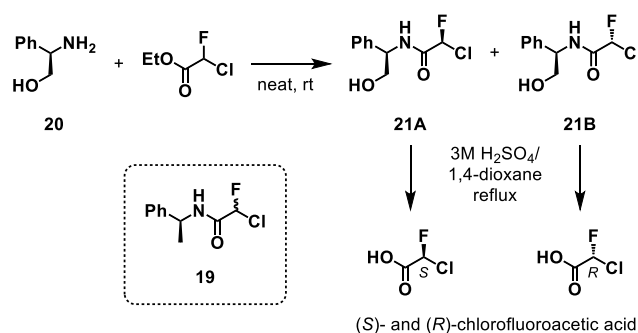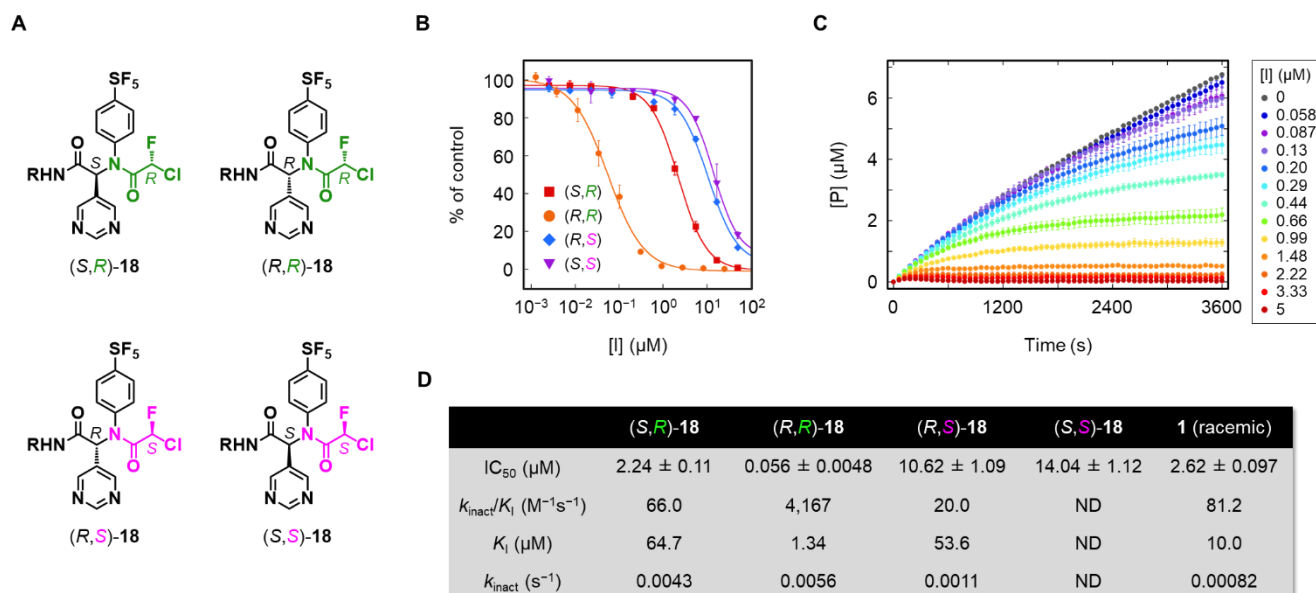


**Scheme 1**. The optical resolution of chlorofluoroacetic acid using (*R*)-(−)-2-phenylglycinol (**20**) as the chiral resolving agent. See Supporting Information for the detail.

Having the isolated stereoisomers of **18** in hand, we evaluated the effect of the chirality of each stereocenter on the M[pro] inhibitory activity (Figure 4). In the fluorescent enzymatic assay, (*R,R*)-**18** (the former *R* indicates the absolute configuration at the Ugi MCR-generated stereocenter, and the latter at CFA) displayed dramatically

higher potency with IC$_{50}$ value of 0.056 μM compared to the others (Figure 4B and 4D). Among the other three isomers, (*S*,*R*)-**18** possessing an (*R*)-CFA warhead showed low micromolar activity (IC$_{50}$ = 2.24 μM), whereas isomers obtained from (*S*)-chlorofluoroacetic acid were weak inhibitors (IC$_{50}$ = 10.62 and 14.04 μM for (*R*,*S*)- and (*S*,*S*)-**18**, respectively). To elucidate how the chirality at CFA affected the inhibitory activity, we performed kinetic analysis of M$^{pro}$ inhibition by (*R*,*R*)-**18** and its diastereomers (*S*,*R*)- and (*R*,*S*)-**18**.[38,39] All three compounds inhibited the hydrolysis of the fluorogenic substrate by M$^{pro}$ in a time-dependent manner, indicative of the irreversible mode of action (Figure 4C and S3–S6). The kinetic parameters for the irreversible inactivation of M$^{pro}$ are summarized in Figure 4D. As expected, (*R*,*R*)-**18** inactivated M$^{pro}$ with much faster rate ($k_{inact}/K_I$ = 4,167 M$^{-1}$s$^{-1}$) than the diastereomers (*S*,*R*)- and (*R*,*S*)-**18** ($k_{inact}/K_I$ = 66.0 and 20.0 M$^{-1}$s$^{-1}$, respectively). (*R*,*R*)- and (*S*,*R*)-**18**, both possessing an (*R*)-CFA warhead, showed similar maximal inactivation rate constant $k_{inact}$ (0.0056 and 0.0043 s$^{-1}$, respectively), whereas the binding constant $K_I$ (describing the concentration required to achieve the half of the inactivation rate of $k_{inact}$) was significantly different (1.34 and 64.7 μM, respectively). The large difference in $K_I$ value by the absolute configuration at the Ugi MCR-generated stereocenter was consistent to the previous studies, where the *R* configuration at this carbon was crucial for the M$^{pro}$ inhibitory activities of ML188 and Jun8-76-3A.[20,21] Comparing (*R*,*R*)- and (*R*,*S*)-**18**, both $k_{inact}$ and $K_I$ values were significantly different. Taken together, these kinetics data demonstrated that the chirality at CFA is important for both in terms of reversible binding and the rate of covalent modification of M$^{pro}$. We also determined the kinetic parameters of acrylamide **1**. Despite the higher intrinsic reactivity of acrylamide toward thiols compared to that of CFA,[31] the $k_{inact}$ value of **1** was significantly smaller than that of (*R*)-CFA and comparable to (*S*)-CFA. This may be due to the acrylamide disposition in **1**–M$^{pro}$ binding complex is not optimal for Michael addition of Cys145.



|  | (*S*,*R*)-**18** | (*R*,*R*)-**18** | (*R*,*S*)-**18** | (*S*,*S*)-**18** | **1** (racemic) |
|---|---|---|---|---|---|
| IC$_{50}$ (μM) | 2.24 ± 0.11 | 0.056 ± 0.0048 | 10.62 ± 1.09 | 14.04 ± 1.12 | 2.62 ± 0.097 |
| $k_{inact}/K_I$ (M$^{-1}$s$^{-1}$) | 66.0 | 4,167 | 20.0 | ND | 81.2 |
| $K_I$ (μM) | 64.7 | 1.34 | 53.6 | ND | 10.0 |
| $k_{inact}$ (s$^{-1}$) | 0.0043 | 0.0056 | 0.0011 | ND | 0.00082 |

**Figure 4**. Comparison of the four stereoisomers of **18**. A) The absolute configurations of each stereoisomer (R = (3-fluorophenyl)ethyl). The *R* and *S* configurations at CFA were highlighted in green and magenta,

respectively. B) Inhibitory activity of each stereoisomer against SARS-CoV-2 M$^{pro}$. Each plot represents the mean of triplicate experiments ± standard deviation. C) Time-course plot of M$^{pro}$-catalyzed hydrolysis of the fluorogenic substrate in the presence of various concentrations of inhibitor ($R,R$)-**18**. Data are represented as the concentration of the product (7-amino-4-methylcoumarin) determined by the fluorescence intensity. Each plot represents the mean of triplicate experiments ± standard error of the mean. D) Summary of IC$_{50}$ values and kinetic parameters. ND, not determined.

 

 

The selectivity of ($R,R$)-**18** toward SARS-CoV-2 M$^{pro}$ was evaluated. We first assessed the inhibitory activity of ($R,R$)-**18** toward other cysteine proteases (Figure 5A). ($R,R$)-**18** potently inhibited SARS-CoV-1 M$^{pro}$ with IC$_{50}$ value of 0.094 μM. This was not surprising because M$^{pro}$ is highly conserved between SARS-CoV-1 and SARS-CoV-2 (96% identity of the amino acid sequence). ($R,R$)-**18** did not inhibit SARS-CoV-2 PL$^{pro}$ (<1% inhibition at 20 μM), indicating its specificity toward M$^{pro}$ between two proteases required for polyprotein processing. We also evaluated the inhibition of two human cysteine proteases, cathepsins B and L. Both proteases were not inhibited by 20 μM of ($R,R$)-**18**, whereas Ugi MCR-generated, noncovalent furan-2-carboxamide compound Jun8-76-3A, moderately inhibited cathepsin B (55% inhibition at 20 μM). To assess the M$^{pro}$ selectivity of CFA dipeptides among the proteome, we designed a clickable activity-based probe (ABP) by replacing the F on the (3-fluorophenyl)ethyl group of ($R,R$)-**18** by an alkyne (Figure 5B). To our delight, the ethynyl moiety was well tolerated and probe **22** exhibited comparable inhibitory activity against SARS-CoV-2 M$^{pro}$ (IC$_{50}$ = 0.11 μM) to that of ($R,R$)-**18** (IC$_{50}$ = 0.056 μM). To test the capability as an ABP, **22** was reacted with recombinant SARS-CoV-2 M$^{pro}$ (37 °C, 1 h) and subsequently conjugated to rhodamine-azide by copper-catalyzed azide–alkyne cycloaddition (CuAAC). The covalent **22**–M$^{pro}$ adduct was visualized by in-gel fluorescence analysis after SDS-PAGE (Figure 5B). The gel image showed that M$^{pro}$ could be detected from as low as 25 nM by 2.5 μM of **22**. M$^{pro}$ (50 nM) was labeled by **22** in a concentration-dependent manner, and the fluorescent intensity reached the plateau at 2.5 μM of **22**. **22** successfully labeled M$^{pro}$ spiked into the lysate of A431 cells (derived from human lung cancer), demonstrating its capability for covalent modification of M$^{pro}$ in the complex human proteome (Figure 5C and S7). We also prepared acrylamide probe **23** based on the structure of **1**, and compared the proteome-wide activity of **22** and **23** under live cell conditions (Figure 5D and S8). A431 cells were treated with **22** or **23** (37 °C, 1 h) and subsequently processed for the visualization of the labeled proteome after cell lysis. Acrylamide **23** exhibited a higher degree of concentration-dependent indiscriminate protein labeling compared to CFA **22**, in concordance to the higher intrinsic reactivity of acrylamide toward thiols than that of CFA. Overall, these data demonstrated that the CFA-dipeptides displayed good selectivity toward M$^{pro}$ and low indiscriminate reactivity in the human cell proteome.
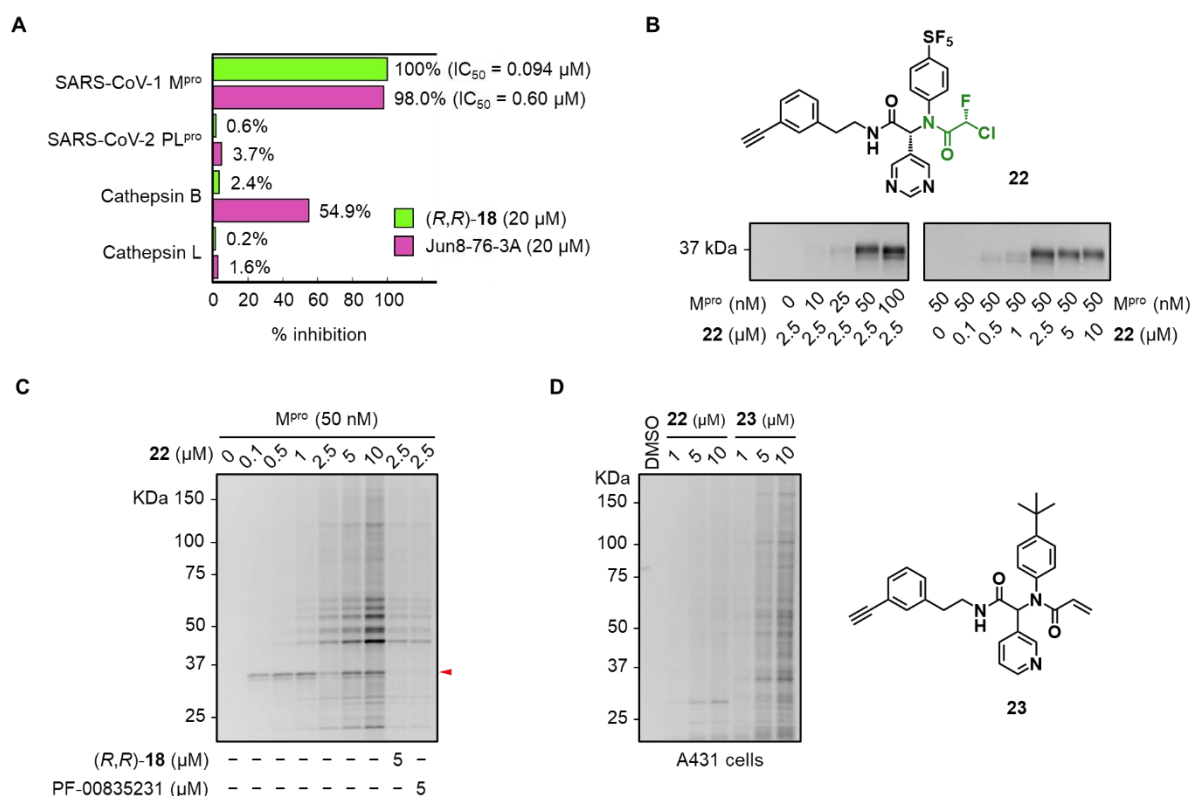
**Figure 5**. Selectivity of CFA-dipeptides toward M$^{pro}$. A) Inhibitory activity of (*R,R*)-**18** and Jun8-76-3A toward other viral and human cysteine proteases. The data are represented as the average of two independent experiments. B) Fluorescent labeling of recombinant SARS-CoV-2 M$^{pro}$ by CFA probe **22**. M$^{pro}$ was reacted with the designated concentration of **22** (37 °C, 1 h) and analyzed by in-gel ABPP after CuAAC with rhodamine azide. C) Reactivity profile of **22** toward M$^{pro}$ spiked into A431 cell lysate (37 °C, 1 h). The samples of right two lanes were preincubated with the designated inhibitor (37 °C, 30 min) before addition of **22**. Red arrow indicates SARS-CoV-2 M$^{pro}$. D) Reactivity profiles of **22** and acrylamide probe **23** toward the live cell proteome of A431 cells (37 °C, 1 h).

## Conclusion

SARS-CoV-2 M$^{pro}$ plays a vital role in the process of viral replication and is an attractive protein target for the development of antiviral agents to treat COVID-19. In this study, we developed a novel irreversible M$^{pro}$ inhibitor utilizing CFA as the warhead for the covalent capture of the catalytic cysteine. Ugi MCR afforded CFA derivatives in one-pot from chlorofluoroacetic acid, aniline, aldehyde, and isocyanide, allowing for rapid screening of the substituents derived from each building block. The diastereomers of CFA derivatives showed significantly different inhibitory activity against M$^{pro}$, suggesting the importance of the chirality at CFA. We established a practical protocol for the optical resolution of chlorofluoroacetic acid, which enabled the isolation of the four stereoisomers of the optimized CFA compound **18** bypassing the use of expensive chiral HPLC. Among the stereoisomers, (*R,R*)-**18** displayed significantly higher M$^{pro}$ inhibitory activity (IC$_{50}$ = 0.056 μM)

than those of the reported noncovalent and covalent inhibitors based on the same Ugi MCR-generated dipeptide scaffold. The kinetic analysis of M[pro] inhibition revealed that the *R* configuration of CFA is crucial for the activity both in terms of binding affinity and the rate of covalent modification of M[pro]. These results indicated that the electrophilic reactivity of CFA could be enhanced under the microenvironment in the active site of M[pro] in a stereospecific manner. (*R*,*R*)-**18** showed high selectivity toward SARS-CoV-1 and SARS-CoV-2 M[pro] among other cysteine proteases, and ABPP experiments using an alkynylated probe **22** demonstrated the low indiscriminate reactivity of CFA toward the human cell proteome. Overall, these data suggest the potential of (*R*,*R*)-**18** as the lead for further development of CFA-based irreversible SARS-CoV-2 M[pro]. More importantly, our findings highlight the prominent influence of the CFA chirality on the covalent modification of the targeted cysteine in the enzyme binding pocket. This would provide an extra opportunity for improving the potency and selectivity in the development of novel CFA-based covalent inhibitors for various cysteine-containing protein targets.

The high electronegativity of fluorine makes C–F bonds highly polarized,[40] and fluorine atom(s) in small molecule ligands can participate in noncovalent interactions with the protein in diverse ways.[41] Assuming the same binding mode of CFA dipeptides in M[pro] active site to the reported Ugi MCR-based inhibitors, we speculate that the fluorine atom of CFA makes hydrogen bonding(s) with the backbone NH of Gly143 and/or Cys145, which are thought to form the oxyanion hole in the S1' pocket.[42] This interaction may determine the orientation of the C–Cl bond of CFA in the binding pocket, rendering (*R*)-CFA more suitable for the $S_N2$ substitution reaction by the cysteine thiol compared to (*S*)-CFA. Computational docking studies are ongoing to examine this possibility in more depth and will be reported in due course.



**Methods**

*Enzymatic Assays*

All cysteine proteases were purchased from BPS Bioscience (San Diego, CA): SARS-CoV-2 main protease (M[pro]) (100823), SARS-CoV-1 M[pro] (100807), SARS-CoV-2 papain-like protease (PL[pro]) (100735), human cathepsin B (80001), and human cathepsin L (80005). All enzymatic assays were performed in 96-well micro plates (PerkinElmer, 6052260). M[pro] enzymatic assays were performed in the reaction buffer containing 20 mM Tris-HCl (pH 7.3), 100 mM NaCl, 1 mM EDTA, and 1 mM DTT. 25 nM SARS-CoV-2 M[pro] or 200 nM SARS-CoV-1 M[pro] (20 μL) and the testing compound at various concentrations (20 μL) were added to each well and incubated for 30 min at ambient temperature. The enzymatic reaction was initiated by adding the fluorogenic substrate (Ac-Abu-Tle-Leu-Gln-MCA, Peptide Institute 3250-v) (50 μM, 10 μL) and allowed to proceed for 6 h at ambient temperature. The fluorescence intensity of each well was measured using PerkinElmer EnSpire multimode plate reader (PerkinElmer) at an excitation wavelength of 355 nm and an emission wavelength of 460 nm. Percent activity or inhibition was calculated based on control wells containing no inhibitor (100% activity/0% inhibition) and blank wells containing no M[pro] (0% activity/100% inhibition) and plotted versus inhibitor concentration. IC$_{50}$ values were generated by curve fitting using KaleidaGraph (Synergy Software). SARS-CoV-2 PL[pro] enzymatic assays were performed in the same reaction buffer to M[pro] enzymatic assays. 500

nM PL$^{pro}$ (20 μL) and the testing compound (125 μM, 20 μL) were added to each well and incubated for 30 min at ambient temperature. The enzymatic reaction was initiated by adding the substrate (Z-Arg-Leu-Arg-Gly-Gly-MCA, Sigma-Aldrich SML2966) (50 μM, 10 μL) and allowed to proceed for 6 h at ambient temperature. Percent inhibition was calculated as described above.

Cathepsin enzymatic assays were performed in the reaction buffer containing 20 mM sodium acetate (pH 5.5), 1 mM EDTA, and 5 mM DTT. 750 pM cathepsin B or 750 pM cathepsin L (20 μL) and the testing compound (125 μM, 20 μL) were added to each well and incubated for 30 min at ambient temperature. The enzymatic reaction was initiated by adding the fluorogenic substrate (Z-Leu-Arg-MCA, Peptide Institute 3210-v) (25 μM, 10 μL) and allowed to proceed for 1 h at ambient temperature. Percent inhibition was calculated as described above.

*$K_m$ determination of Ac-Abu-Tle-Leu-Gln-MCA*

$K_m$ value of SARS-CoV-2 M$^{pro}$ for the fluorogenic substrate Ac-Abu-Tle-Leu-Gln-MCA was determined at 12 different substrate concentrations ranging from 156.3 to 2.6 μM. 20 nM M$^{pro}$ solution (25 μL) was added to each well of a 96-well plate. The enzymatic reaction was initiated by adding substrate solution (25 μL) and allowed to proceed for 20 min at 37 °C. The product formation was continuously monitored using PerkinElmer EnSpire multimode plate reader at an excitation wavelength of 355 nm and an emission wavelength of 460 nm. The rate of the product formation was plotted versus the substrate concentration, and $K_m$ value was obtained by non-linear regression using the Michaelis–Menten equation (Figure S9). $K_m$ value of 126.8 μM was obtained for Ac-Abu-Tle-Leu-Gln-MCA and used to determine the kinetic parameters for the irreversible inactivation of SARS-CoV-2 M$^{pro}$.

*Determination of the kinetic parameters for M$^{pro}$ inactivation*

125 μM Ac-Abu-Tle-Leu-Gln-MCA (20 μL) and the inhibitor at various concentrations (20 μL) were added to each well of 96-well microplates. The enzymatic reaction was initiated by adding 50 nM SARS-CoV-2 M$^{pro}$ (10 μL) and allowed to proceed for 60 min at 37 °C. The fluorescence intensity was continuously measured using PerkinElmer EnSpire multimode plate reader at an excitation wavelength of 355 nm and an emission wavelength of 460 nm. The raw fluorescence data were zero-corrected by subtracting the fluorescence value at 0 sec and converted to product concentration [P] using a calibration curve obtained by 7-amino-4-methylcoumarin. [P] was plotted versus time and the initial state velocity $v_i$ at each inhibitor concentration was determined by linear regression of the initial three data points. The observed first-order rate constant $k_{obs}$ at each inhibitor concentration was determined by non-linear regression using equation (1). The second-order rate constant $k_{inact}/K_I$ was determined by plotting $k_{obs}$ versus [I] and non-linear regression using equation (2). The $v_i$ values were plotted against [I]/(1 + [S]/$K_m$) and non-linear regression using equation (3) afforded $K_I$ value, where $v_0$ is the rate in the absence of the inhibitor. The $k_{inact}$ value was calculated from the $k_{inact}/K_I$ and $K_I$ values.

357 $$[P] = \frac{v_i}{k_{obs}}\left(1 - e^{(-k_{obs}t)}\right) + \text{offset} \qquad (1)$$

358

360 $$k_{\text{obs}} = \frac{k_{\text{inact}} \times [I]}{[I] + K_{\text{I}}(1 + [S]/K_{\text{m}})} \qquad (2)$$

359

362 $$v_i = \frac{v_0}{1 + [I]/K_{\text{I}}} \qquad (3)$$

361

363

364 *SARS-CoV-2 M<sup>pro</sup> labeling and in-gel fluorescence analysis*

365 Recombinant SARS-CoV-2 M$^{pro}$ was diluted in the buffer containing 50 mM HEPES (pH7.5), 150 mM NaCl,

366 and 1 mM DTT. DMSO solution of **22** was diluted in the same buffer, and 25 μL each of M$^{pro}$ and **22** solution

367 in buffer was combined to initiate the reaction. After incubated for 1 h at 37 °C, to the mixture was added 100

368 mM *N*-ethylmaleimide solution (1 μL) and further incubated for 20 min. The reaction mixture was subjected to

369 copper-catalyzed azide–alkyne cycloaddition (CuAAC) reaction with 16.5 μM rhodamine azide, 0.8 mM TCEP

370 (Sigma-Aldrich), 80 μM tris(3-hydroxypropyltriazolylmethyl)amine (THPTA, TCI) and 1.25 mM CuSO$_4$. The

371 mixture was incubated for 1 h at 37 °C. After addition of 15 μL 5×SDS-PAGE loading buffer, the mixture was

372 boiled for 5 min at 95 °C and each sample (12 μL) was resolved on 5-15% SDS-PAGE gel (Nacalai tesque).

373 The in-gel fluorescence was analyzed using LAS-4000 lumino image analyzer (Fujifilm).

374

375 *SARS-CoV-2 M<sup>pro</sup> labeling in A431 cell lysate*

376 A431 cells were purchased from the American Type Culture Collection (ATCC, VA) and grown at 37 °C under

377 a humidified 5% CO$_2$ atmosphere in a culture medium containing low-glucose DMEM (Gibco) supplemented

378 with 10% FBS (HyClone), penicillin (50 IU/mL) and streptomycin (50 μg/mL). The cells were grown to ~90%

379 confluence in 10 mL of growth medium in 100-mm culture dishes (Corning Primaria). The medium was

380 aspirated off, and the cells were washed twice with DPBS (10 mL). To culture dishes were added the buffer

381 containing 50 mM HEPES (pH7.5), 150 mM NaCl, and 1 mM DTT (1 mL), and the cells were harvested using

382 a plastic scraper in DPBS and collected by centrifugation (4 °C, 200*g*, 5 min), and the supernatant was removed.

383 The pellets were resuspended in the ice-cold buffer (200 μL) and lysed using a probe sonicator. The suspension

384 was centrifuged (4 °C, 17,730*g*, 10 min) and the supernatant was collected for use as lysate.

385 Protein concentration of the lysate was determined using DC protein assay kit (BioRad) and normalized to 0.4

386 mg/mL by dilution with the buffer. Different concentrations of SARS-CoV-2 M$^{pro}$ was spiked into the lysate and

387 treated with **22** and processed for in-gel fluorescence analysis as described above. For competition experiments,

388 the lysate spiked with M$^{pro}$ was preincubated with the designated inhibitor for 30 min at 37 °C before adding **22**.

389

390

391    *Protein labeling in live A431 cells*

392    A431 cells were grown to ~80% confluence in 4 mL of growth medium in 60-mm culture dishes (Corning

393    Primaria). The growth medium was aspirated off, and the cells were washed twice with DPBS (3 mL), followed

394    by treatment with **22** in culture medium (4 mL, FBS(−)). After incubation at 37 °C in a $CO_2$ incubator for 1 h,

395    the medium was aspirated off. The cells were washed twice with cold DPBS (3 mL) and lysed with cold RIPA

396    buffer (50mM Tris-HCl pH 7.6, 150mM NaCl, 1w/v% Nonidet P40 substitute, 0.5w/v% sodium deoxycholate,

397    0.1w/v% SDS, 50 μL) containing protease inhibitor cocktail (Roche) and *N*-ethylmaleimide (2 mM). The lysed

398    cells were collected using a plastic scraper, transferred to a microfuge tube, and centrifuged (4 °C, 17,730*g*, 10

399    min). The supernatant was transferred to a microfuge tube and stored at −30 °C.

400    The cell lysates were thawed on ice. Protein concentrations of each sample were determined using DC protein

401    assay kit (BioRad) and normalized to 0.5 mg/mL (A431 cells) by dilution with DPBS. The solution (52 μL) was

402    subjected to CuAAC, SDS-PAGE, and in-gel fluorescence analysis as described for $M^{pro}$ labeling.

403

404

414

415

## References

1. F. Wu, S. Zhao, B. Yu, Y.-M. Chen, W. Wang, Z.-G. Song, Y. Hu, Z.-W. Tao, J.-H. Tian, Y.-Y. Pei, M.-L. Yuan, Y.-L. Zhang, F.-H. Dai, Y. Liu, Q.-M. Wang, J.-J. Zheng, L. Xu, E. C. Holmes, Y.-Z. Zhang, A new coronavirus associated with human respiratory disease in China, *Nature* **2020**, *579*, 265–269.

2. P. Zhou, X.-L. Yang, X.-G. Wang, B. Hu, L. Zhang, W. Zhang, H.-R. Si, Y. Zhu, B. Li, C.-L. Huang, H.-D. Chen, J. Chen, Y. Luo, H. Guo, R.-D. Jiang, M.-Q. Liu, Y. Chen, X.-R. Shen, X. Wang, X.-S. Zheng, K. Zhao, Q.-J. Chen, F. Deng, L.-L. Liu, B. Yan, F.-X. Zhan, Y.-Y. Wang, G.-F. Xiao, Z.-L. Shi, A pneumonia outbreak associated with a new coronavirus of probable bat origin. *Nature* **2020**, *579*, 270–273.

3. W. T. Harvey, A. M. Carabelli, B. Jackson, R. K. Gupta, E. C. Thomson, E. M. Harrison, C. Ludden, R. Reeve, A. Rambaut, C. G. U. Consortium, S. J. Peacock, D. L. Robertson, SARS-CoV-2 variants, spike mutations and immune escape, *Nat. Rev. Microbiol.* **2021**, *19*, 409–424.

4. C. Gil, T. Ginex, I. Maestro, V. Nozal, L. Barrado-Gil, M. Á. Cuesta-Geijo, J. Urquiza, D. Ramírez, C. Alonso, N. E. Campillo, A. Martinez, COVID-19: Drug Targets and Potential Treatments, *J. Med. Chem.* **2020**, *63*, 12359–12386.

5. T. Pillaiyar, S. Meenakshisundaram, M. Manickam, *Drug Discov. Today* **2020**, *25*, 668–688.

6. R. Cannalire, C. Cerchia, A. R. Beccari, F. S. Di Leva, V. Summa, Targeting SARS-CoV-2 Proteases and Polymerase for COVID-19 Treatment: State of the Art and Future Opportunities. *J. Med. Chem.* **2021**, https://doi.org/10.1021/acs.jmedchem.0c01140.

7. Z. Jin, X. Du, Y. Xu, Y. Deng, M. Liu, Y. Zhao, B. Zhang, X. Li, L. Zhang, C. Peng, Y. Duan, J. Yu, L. Wang, K. Yang, F. Liu, R. Jiang, X. Yang, T. You, X. Liu, X. Yang, F. Bai, H. Liu, X. Liu, L. W. Guddat, W. Xu, G. Xiao, C. Qin, Z. Shi, H. Jiang, Z. Rao, H. Yang, *Nature* **2020**, *582*, 289–293.

8. W. Rut, K. Groborz, L. Zhang, X. Sun, M. Zmudzinski, B. Pawlik, X. Wang, D. Jochmans, J. Neyts, W. Młynarski, R. Hilgenfeld, M. Drag, SARS-CoV-2 M$^{pro}$ inhibitors and activity-based probes for patient-sample imaging. *Nat. Chem. Biol.* **2021**, *17*, 222–228.

9. K. Anand, J. Ziebuhr, P. Wadhwani, J. R. Mesters, R. Hilgenfeld, *Science* **2003**, *300*, 1763–1767.

10. A. Wu, Y. Wang, C. Zeng, X. Huang, S. Xu, C. Su, M. Wang, Y. Chen, D. Guo, Prediction and biochemical analysis of putative cleavage sites of the 3C-like protease of Middle East respiratory syndrome coronavirus. *Virus Res.* **2015**, *208*, 56–65.

11. L. Zhang, D. Lin, X. Sun, U. Curth, C. Drosten, L. Sauerhering, S. Becker, K. Rox, R. Hilgenfeld, Crystal structure of SARS-CoV-2 main protease provides a basis for design of improved α-ketoamide inhibitors. *Science* **2020**, *368*, 409–412.

12. W. Dai, B. Zhang, X.-M. Jiang, H. Su, J. Li, Y. Zhao, X. Xie, Z. Jin, J. Peng, F. Liu, C. Li, Y. Li, F. Bai, H. Wang, X. Cheng, X. Cen, S. Hu, X. Yang, J. Wang, X. Liu, G. Xiao, H. Jiang, Z. Rao, L.-K. Zhang, Y. Xu, H. Yang, H. Liu, Structure-based design of antiviral drug candidates targeting the SARS-CoV-2 main protease. *Science* **2020**, *368*, 1331–1335.

13. J. Qiao, Y.-S. Li, R. Zeng, F.-L. Liu, R.-H. Luo, C. Huang, Y.-F. Wang, J. Zhang, B. Quan, C. Shen, X. Mao, X. Liu, W. Sun, W. Yang, X. Ni, K. Wang, L. Xu, Z.-L. Duan, Q.-C. Zou, H.-L. Zhang, W. Qu, Y.-H.-P. Long, M.-H. Li, R.-C. Yang, X. Liu, J. You, Y. Zhou, R. Yao, W.-P. Li, J.-M. Liu, P. Chen, Y. Liu, G.-F. Lin,

X. Yang, J. Zou, L. Li, Y. Hu, G.-W. Lu, W.-M. Li, Y.-Q. Wei, Y.-T. Zheng, J. Lei, S. Yang, SARS-CoV-2 M$^{pro}$ inhibitors with antiviral activity in a transgenic mouse model. *Science* **2021**, *371*, 1374–1378.

14. K. S Yang, X. R. Ma, Y. Ma, Y. R. Alugubelli, D. A. Scott, E. C. Vatansever, A. K. Drelich, B. Sankaran, Z. Z. Geng, L. R. Blankenship, H. E. Ward, Y. J. Sheng, J. C. Hsu, K. C. K, B. Zhao, H. S. Hayatshahi, J. Liu, P. Li, C. A. Fierke, C.-T. K. Tseng, S. Xu, W. R. Liu, A Quick Route to Multiple Highly Potent SARS-CoV-2 Main Protease Inhibitors. *ChemMedChem* **2021**, *16*, 942–948.

15. W. Dai, D. Jochmans, H. Xie, H. Yang, J. Li, H. Su, D. Chang, J. Wang, J. Peng, L. Zhu, Y. Nian, R. Hilgenfeld, H. Jiang, K. Chen, L. Zhang, Y. Xu, J. Neyts, H. Liu, Design, Synthesis, and Biological Evaluation of Peptidomimetic Aldehydes as Broad-Spectrum Inhibitors against Enterovirus and SARS-CoV-2. *J. Med. Chem.* **2021**, https://doi.org/10.1021/acs.jmedchem.0c02258

16. R. L. Hoffman, R. S. Kania, M. A. Brothers, J. F. Davies, R. A. Ferre, K. S. Gajiwala, M. He, R. J. Hogan, K. Kozminski, L. Y. Li, J. W. Lockner, J. Lou, M. T. Marra, L. J. Mitchell, B. W. Murray, J. A. Nieman, S. Noell, S. P. Planken, T. Rowe, K. Ryan, G. J. Smith, J. E. Solowiej, C. M. Steppan, B. Taggart, Discovery of Ketone-Based Covalent Inhibitors of Coronavirus 3CL Proteases for the Potential Therapeutic Treatment of COVID-19. *J. Med. Chem.* **2020**, *63*, 12725–12747.

17. S. Hattori, N. Higashi-Kuwata, H. Hayashi, S. R. Allu, J. Raghavaiah, H. Bulut, D. Das, B. J. Anson, E. K. Lendy, Y. Takamatsu, N. Takamune, N. Kishimoto, K. Murayama, K. Hasegawa, M. Li, D. A. Davis, E. N. Kodama, R. Yarchoan, A. Wlodawer, S. Misumi, A. D. Mesecar, A. K. Ghosh, H. Mitsuya, A small molecule compound with an indole moiety inhibits the main protease of SARS-CoV-2 and blocks virus replication. *Nat. Commun.* **2021**, *12*, No. 668.

18. B. Bai, A. Belovodskiy, M. Hena, A. S. Kandadai, M. A. Joyce, H. A. Saffran, J. A. Shields, M. B. Khan, E. Arutyunova, J. Lu, S. K. Bajwa, D. Hockman, C. Fischer, T. Lamer, W. Vuong, M. J. van Belkum, Z. Gu, F. Lin, Y. Du, J. Xu, M. Rahim, H. S. Young, J. C. Vederas, D. L. Tyrrell, M. J. Lemieux, J. A. Nieman, *J. Med. Chem.* **2021**, https://doi.org/10.1021/acs.jmedchem.1c00616.

19. S. Konno, K. Kobayashi, M. Senda, Y. Funai, Y. Seki, I. Tamai, L. Schäkel, K. Sakata, T. Pillaiyar, A. Taguchi, A. Taniguchi, M. Gütschow, C. E. Müller, K. Takeuchi, M. Hirohama, A. Kawaguchi, M. Kojima, T. Senda, Y. Shirasaka, W. Kamitani, Y. Hayashi, *J. Med. Chem.* **2021**, https://doi.org/10.1021/acs.jmedchem.1c00665.

20. J. Jacobs, V. Grum-Tokars, Y. Zhou, M. Turlington, S. A. Saldanha, P. Chase, A. Eggler, E. S. Dawson, Y. M. Baez-Santos, S. Tomar, A. M. Mielech, S. C. Baker, C. W. Lindsley, P. Hodder, A. Mesecar, S. R. Stauffer, Discovery, Synthesis, And Structure-Based Optimization of a Series of *N*-(tert-Butyl)-2-(*N*-arylamido)-2-(pyridin-3-yl) Acetamides (ML188) as Potent Noncovalent Small Molecule Inhibitors of the Severe Acute Respiratory Syndrome Coronavirus (SARS-CoV) 3CL Protease. *J. Med. Chem.* **2013**, *56*, 534–546.

21. N. Kitamura, M. D. Sacco, C. Ma, Y. Hu, J. A. Townsend, X. Meng, F. Zhang, X. Zhang, M. Ba, T. Szeto, A. Kukuljac, M. T. Marty, D. Schultz, S. Cherry, Y. Xiang, Y. Chen, J. Wang, *J. Med. Chem.* **2021**, https://doi.org/10.1021/acs.jmedchem.1c00509.

22. D. Zaidman, P. Gehrtz, M. Filep, D. Fearon, R. Gabizon, A. Douangamath, J. Prilusky, S. Duberstein, G.

Cohen, C. D. Owen, E. Resnick, C. Strain-Damerell, P. Lukacik, C.-M. Consortium; H. Barr, M. A. Walsh, F. von Delft, N. London, An automatic pipeline for the design of irreversible derivatives identifies a potent SARS-CoV-2 M<sup>pro</sup> inhibitor. *Cell Chem. Biol.* **2021**, https://doi.org/10.1016/j.chembiol.2021.05.018.

23. J. Singh, R. C. Petter, T. A. Baillie, A. Whitty, The Resurgence of Covalent Drugs. *Nat. Rev. Drug. Discov.* **2011**, *10*, 307–317.

24. F. M. Ferguson, N. S. Gray, Kinase inhibitors: the road ahead. *Nat. Rev. Drug Discov.* **2018**, *17*, 353–377.

25. D. Kim, J. Y. Xue, P. Lito, Targeting KRAS(G12C): From Inhibitory Mechanism to Modulation of Antitumor Effects in Patients. *Cell* **2020**, *183*, 850–859.

26. U. P. Dahal, R. S. Obach, A. M. Gilbert, Benchmarking *in Vitro* Covalent Binding Burden As a Tool To Assess Potential Toxicity Caused by Nonspecific Covalent Binding of Covalent Drugs. *Chem. Res. Toxicol.* **2013**, *26*, 1739–1745.

27. E. Mons, R. Q. Kim, B. R. van Doodewaerd, P. A. van Veelen, M. P. C. Mulder, H. Ovaa, Exploring the Versatility of the Covalent Thiol-Alkyne Reaction with Substituted Propargyl Warheads: A Deciding Role for the Cysteine Protease. *J. Am. Chem. Soc.* **2021**, *143*, 6423–6433.

28. D. E. Mortenson, G. J. Brighty, L. Plate, G. Bare, W. Chen, S. Li, H. Wang, B. F. Cravatt, S. Forli, E. T. Powers, K. B. Sharpless, I. A. Wilson, J. W. Kelly, "Inverse Drug Discovery" Strategy to Identify Proteins That Are Targeted by Latent Electrophiles as Exemplified by Aryl Fluorosulfates. *J. Am. Chem. Soc.* **2018**, *140*, 200–221.

29. J. M. Bradshaw, J. M. McFarland, V. O. Paavilainen, A. Bisconte, D. Tam, V. T. Phan, S. Romanov, D. Finkle, J. Shu, V. Patel, T. Ton, X. Li, D. G. Loughhead, P. A. Nunn, D. E. Karr, M. E. Gerritsen, J. O. Funk, T. D. Owens, E. Verner, K. A. Brameld, R. J. Hill, D. M. Goldstein, J. Taunton, Prolonged and tunable residence time using reversible covalent kinase inhibitors. *Nat. Chem. Biol.* **2015**, *11*, 525–531.

30. P. M. Cal, J. B. Vicente, E. Pires, A. V. Coelho, L. F. Veiros, C. Cordeiro, P. M. Gois, Iminoboronates: a new strategy for reversible protein modification. *J. Am. Chem. Soc.* **2012**, *134*, 10299–10305.

31. N. Shindo, H. Fuchida, M. Sato, K. Watari, T. Shibata, K. Kuwata, C. Miura, K. Okamoto, Y. Hatsuyama, K. Tokunaga, S. Sakamoto, S. Morimoto, Y. Abe, M. Shiroishi, J. M. M. Caaveiro, T. Ueda, T. Tamura, N. Matsunaga, T, Nakao, S. Koyanagi, S. Ohdo, Y. Yamaguchi, I. Hamachi, M. Ono, A. Ojida, Selective and Reversible Modification of Kinase Cysteines with Chlorofluoroacetamides. *Nat. Chem. Biol.* **2019**, *15*, 250−258.

32. M. Sato, H. Fuchida, N. Shindo, K. Kuwata, K. Tokunaga, X.-L. Guo, R. Inamori, K. Hosokawa, K. Watari, T. Shibata, N. Matsunaga, S. Koyanagi, S. Ohdo, M. Ono, A. Ojida, Selective Covalent Targeting of Mutated EGFR(T790M) with Chlorofluoroacetamide-Pyrimidines. *ACS Med. Chem. Lett.* **2020**, *11*, 1137−1144.

33. C. Miura, N. Shindo, K. Okamoto, K. Kuwata, A. Ojida, Fragment-Based Discovery of Irreversible Covalent Inhibitors of Cysteine Proteases Using Chlorofluoroacetamide Library. *Chem. Pharm. Bull.* **2020**, *68*, 1074−1081.

34. C.-J. Kuo, Y.-H. Chi, J. T.-A. Hsu, P.-H. Liang, Characterization of SARS main protease and inhibitor assay using a fluorogenic substrate. *Biochem. Biophys. Res. Commun.* **2004**, *318*, 862−867.

35. M. F. Sowaileh, R. A. Hazlitt, D. A. Colby, Application of the Pentafluorosulfanyl Group as a Bioisosteric Replacement. *ChemMedChem* **2017**, *12*, 1481−1490.

36. G. Bellucci, G. Berti, A. Borraccini, F. Macchia, The preparation of optically active chlorofluoroacetic acid and chlorofluoroethanol. *Tetrahedron* **1969**, *25*, 2979−2985.

37. H. Molines, C. Wakselman, *Synthesis* **1984**, *1984*, 838−839.

38. P. J. Tonge, Quantifying the Interactions between Biomolecules: Guidelines for Assay Design and Data Analysis. *ACS Infect. Dis.* **2019**, *5*, 796−808.

39. J. Breidenbach, C. Lemke, T. Pillaiyar, L. Schäkel, G. Al Hamwi, M. Diett, R. Gedschold, N. Geiger, V. Lopez, S. Mirza, V. Namasivayam, A. C. Schiedel, K. Sylvester, D. Thimm, C. Vielmuth, L. P. Vu, M. Zyulina, J. Bodem, M. Gütschow, C. E. Müller, Targeting the Main Protease of SARS-CoV-2: From the Establishment of High Throughput Screening to the Design of Tailored Inhibitors. *Angew. Chem. Int. Ed.* **2021**, *60*, 10423−10429.

40. D. O'Hagan, Understanding organofluorine chemistry. An introduction to C−F bond. *Chem. Soc. Rev.* **2008**, *37*, 308−319.

41. P. Zhou, J. Zhou, F. Tian, Z. Shang, Fluorine Bonding − How Does It Work In Protein−Ligand Interactions? *J. Chem. Inf. Model.* **2009**, *49*, 2344−2355.

42. J. Lee, L. J. Worrall, M. Vuckovic, F. I. Rosell, F, Gentile, A.-T. Ton, N. A. Caveney, F. Ban, A. Cherkasov, M. Paetzel, N. C. Strynadka, Crystallographic structure of wild-type SARS-CoV-2 main protease acyl-enzyme intermediate with physiological C-terminal autoprocessing site. *Nat. Commun.* **2020**, *11*, No. 5877.